UC San Diego

UC San Diego Previously Published Works

Title

Detecting stress injury (fatigue fracture) in fibular cortical bone using quantitative ultrashort echo time-magnetization transfer (UTE-MT): An ex vivo study

Permalink

https://escholarship.org/uc/item/3nt219g5

Journal

NMR in Biomedicine, 31(11)

ISSN

0952-3480

Authors

Jerban, Saeed
Ma, Yajun
Nazaran, Amin
et al.

Publication Date

2018-11-01

DOI

10.1002/nbm.3994

Peer reviewed

eScholarship.org Powered by the California Digital Library
University of California

Received: 29 September 2017 | Revised: 3 May 2018 | Accepted: 11 June 2018

DOI: 10.1002/nbm.3994

RESEARCH ARTICLE

WILEY NMR IN BIOMEDICINE

Detecting stress injury (fatigue fracture) in fibular cortical bone using quantitative ultrashort echo time-magnetization transfer (UTE-MT): An ex vivo study

Saeed Jerban[1] | Yajun Ma[1] | Amin Nazaran[1] | Erik W. Dorthe[2] | Esther Cory[3] | Michael Carl[4] | Darryl D'Lima[2] | Robert L. Sah[3,5] | Eric Y. Chang[1,6] | Jiang Du[1]

[1] Department of Radiology, University of California, San Diego, California

[2] Shiley Center for Orthopedic Research and Education at Scripps Clinic, La Jolla, California

[3] Department of Bioengineering, University of California, San Diego, La Jolla, California

[4] GE Healthcare, San Diego, California

[5] Department of Orthopedic Surgery, University of California, San Diego, La Jolla, California

[6] Radiology Service, VA San Diego Healthcare System, San Diego, California

Correspondence
Jiang Du and Saeed Jerban, Department of Radiology, University of California, 9500 Gilman Dr., San Diego, CA 92093, USA.
Email: jiangdu@ucsd.edu; sjerban@ucsd.edu

Funding information
VA, Grant/Award Number: I01CX001388; National Institutes of Health (NIH), Grant/Award Numbers: 1 R01 AR068987-01, 1 R01 AR062581-01A1 and 5 P01 AG007996

Bone stress injury (BSI) incidents have been increasing amongst athletes in recent years as a result of more intense sporting activities. Cortical bone in the tibia and fibula is one of the most common BSI sites. Nowadays, clinical magnetic resonance imaging (MRI) is the recommended technique for BSI diagnosis at an early stage. However, clinical MRI focuses on edema observations in surrounding soft tissues, rather than the injured components of the bone. Specifically, both normal and injured bone are invisible in conventional clinical MRI. In contrast, ultrashort echo time (UTE)-MRI is able to detect the rapidly decaying signal from the bone. This study aimed to employ UTE-MRI for fatigue fracture detection in fibula cortical bone through an ex vivo investigation. Fourteen human fibular samples (47 ± 20 years old, four women) were subjected to cyclic loading on a four-point bending setup. The loading was displacement controlled to induce −5000 ± 1500 μ-strain at 4 Hz. Loading was stopped when bone stiffness was reduced by 20%. Fibula samples were imaged twice, using UTE-MRI and micro-computed tomography (μCT), first pre-loading and second post-loading. After loading, the macromolecular fraction (MMF) from UTE-MT modeling demonstrated a significant decrease (12% ± 20%, P = 0.02) on average. Single-component T_2^* also decreased significantly by BSI (12% ± 11%, P = 0.01) on average. MMF reduction is hypothesized to be a result of collagenous matrix rupture and water increase. However, faster T_2^* decay might be a result of water shifts towards newly developed microcracks with higher susceptibility. Despite this good sensitivity level of the UTE-MRI technique, the μCT-based porosity at a voxel size of 9 μm was not affected by loading. UTE-MRI shows promise as a new quantitative technique to detect BSI.

KEYWORDS

bone stress injury, cortical bone, fatigue fracture, magnetization transfer, MRI, ultrashort TE

Abbreviations used: μCT, micro-computed tomography; 3D, three-dimensional; 3D-IR-UTE, three-dimensional adiabatic inversion recovery ultrashort echo time; 3D-UTE, three-dimensional ultrashort echo time; BSI, bone stress injury; CT, computed tomography; FA, flip angle;; FOV, field of view; IR, inversion recovery; MMF, macromolecular fraction; MR, magnetic resonance; MRI, magnetic resonance imaging; mRP, modified rectangular pulse; MT, magnetization transfer; MTR, magnetization transfer ratio; PBS, phosphate-buffered saline; RF, radiofrequency; ROI, region of interest; T/R, transmit/receive; TE, echo time; TR, repetition time

 © 2018 John Wiley & Sons, Ltd.

1 | INTRODUCTION

Bone stress injury (BSI) is commonly seen in highly active individuals.[1-5]. In elite athletes, the incidence rate of BSI has been increasing because of longer and more intense sporting activities.[6] Fatigue, insufficiency, pseudo, overuse, exhaustion and marching fractures are other terms used in the literature for BSI.[7,8] Major factors leading to BSI include training cycles, bone health, gender, diet, biomechanics and footwear.[5,8-12]

BSI is initiated by repeated submaximal mechanical loads and results in load-related pain.[1-4,13]. BSI generally occurs in a few weeks after the commencement of intense training.[1] The pain develops gradually in BSI, first presenting only during loading and later occurring also at rest.[1] The incidence rate of BSI correlates highly with cumulative running in athletes.[14]

Bone remodeling, driven by mechanical loading, is continuously orchestrating the bone microstructure. From a biomechanical point of view, the interplay between (1) the high number of load cycles,[15] (2) muscle exhaustion,[5,16] (3) accelerated bone resorption process[1] and (4) local temporal hypoxia[4] ends in BSI. Specifically, all mentioned phenomena may end in ruptures in the collagenous matrix and the occurrence of a set of cracks from hundreds of nanometers to tens of micrometers in size.[17,18]

The common locations of BSI are highly related to the type of exercise.[1-4,16] The long bones of the lower limbs (tibia and fibula) are common sites of BSI occurrence in basketball players and runners.[2,3,5,19-21] The tibia itself accounts for 40%–60% of cases of BSI in runners.[4,6,16]. BSI in the fibula presents similar characteristics, yet with a lower rate of incidence (6%–24% of lower limb BSIs) compared with tibial BSI.[2] In theory, all long bones are susceptible to BSI because of their similar underlying anatomical morphology and biomechanics.

The early-stage diagnosis of BSI is crucial for the optimization of treatment and return to play time. In competitive athletes, the return to play time ranges from weeks to months.[5] A premature return to activity may increase the risk of recurrent BSI.[11] BSI should be distinguished from bone stress reactions that are normally accompanied with some edema, yet display a different set of characteristics. Physical examination is the first step towards the diagnosis of BSI; however, imaging modalities are crucial to confirm the BSI status. Conventional radiography, computed tomography (CT), musculoskeletal ultrasonography, scintigraphy and magnetic resonance imaging (MRI) are common techniques to diagnose BSI.[1,6,13,16,22-24]

Since the late 1990s, clinical MRI has become the most common modality for the early-stage diagnosis of BSI.[1,6,13,16,22-26] Clinical T_1- and T_2-weighted images are recognized as the most practical techniques for the detection of BSI during the first 3 weeks of onset[1,13] through edema detection in periosteum and bone marrow.[1,10,13,27,28] Nevertheless, clinical MRI lacks any quantitative assessment of the injured components of the bone, because normal and injured bones are "invisible" on clinical MRI. Specifically, cortical bone possesses a very short T_2*, such that clinical MRI renders cortical bone with a very low signal, similar to the background.[29,30] Consequently, an MRI-based quantitative assessment of the injured bone is of great interest to orthopedic researchers and surgeons, which can improve the early-stage diagnosis and quantification of BSI, as well as longitudinal follow-up, in athletes recovering from BSI.

Ultrashort echo time-MRI (UTE-MRI) sequences can be used to image and quantitatively assess cortical bone,[29-39] as well as other musculoskeletal tissues, such as tendon and cartilage.[29,40] UTE-MRI can detect signal from both bound water and pore water in cortical bone.[29,30,32,35,36] T_2* of bound water is approximately one-tenth of T_2* of pore water in cortical bone,[29,30,32,35] which enables the separation of bound and pore water using bi-component modeling of the UTE-T_2* signal decay. Bound water can also be selectively imaged via an inversion recovery-UTE (IR-UTE) sequence by inverting and then nulling the signal from pore water.[37,39,41-43]. Figure 1 shows an exemplary axial image of the leg of a healthy volunteer from a clinical gradient echo sequence compared with UTE and IR-UTE sequences. Despite the signal void of the tibial and fibular cortex on clinical MRI (Figure 1A), UTE-MRI and IR-UTE-MRI demonstrate a high signal and contrast in cortical bone (Figure 1A,B). Moreover, magnetization transfer (MT) imaging combined with the UTE technique can be used for the systematic evaluation of the MT effects in bone, including macromolecular fraction (MMF) and macromolecular T_2 (T_{2MM}) obtained from two-pool MT modeling.[33,44] Although UTE-MRI techniques have been used extensively to assess cortical bone,[30,34,41,42,45-50] the changes in UTE-MRI properties following BSI are yet to be investigated.

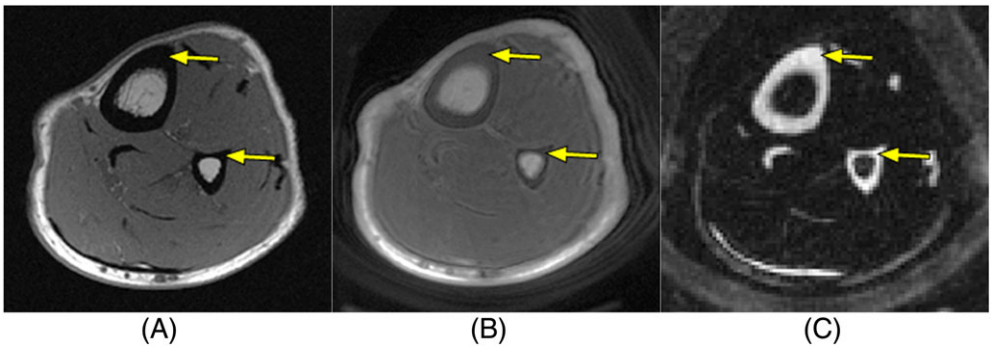

FIGURE 1 Axial magnetic resonance images of the leg of a healthy volunteer. A, Clinical gradient echo sequence shows signal void in the tibial and fibular cortices (arrows). B, Ultrashort echo time (UTE) sequence with an echo time of 32 μs shows a high signal in cortical bone (arrow). C, Inversion recovery (IR)-UTE sequence provides high contrast for the short T_2* components of cortical bone (arrow) by selective suppression of the signal from fat and muscle

The main objective of this study was to determine whether UTE-MRI biomarkers are sensitive to changes induced by BSI, such as cortical bone microcracks and collagen fibril ruptures. An experimental protocol was planned to create limited fatigue fractures, resembling early-stage BSI, in the midshaft of human fibulae. The investigated biomarkers include UTE-T_2*, T_1 and two-pool MT modeling analyses.

2 | MATERIALS AND METHODS

2.1 | Sample preparation

Cortical bone samples were harvested from the midshaft fibulae of 14 fresh-frozen donors (47 ± 20 years old, four women) obtained from a non-profit whole-body donation company (United Tissue Network, Phoenix, AZ). The donor's lower legs underwent one freezing and thawing cycle. Fibulae midshafts were cut into 4-cm lengths using a bandsaw (Shopmaster, Delta Machinery, Jackson, TN). Bone marrow and trabeculae were gently cleaned with a scalpel from cortical bone. All samples were initially scanned using UTE-MRI as described in Section 2.2. The samples were scanned again after they had undergone a cyclic loading experiment to induce fatigue fractures representing 20% reduction in bone stiffness (Section 2.4).

2.2 | UTE-MRI

All fibular samples were immersed in phosphate-buffered saline (PBS) for 2 hours at room temperature before the MRI scans. Each sample was placed in a 30-mL syringe, filled with perfluoropolyether (Fomblin, Ausimont, Thorofare, NJ) to minimize dehydration and susceptibility artifact. The specimens were imaged in the sagittal plane on a 3-T clinical MRI scanner (Signa HDx, GE Healthcare Technologies, Milwaukee, WI) using a home-made 1-in-diameter solenoid transmit/receive (T/R) coil. A quantitative imaging protocol was performed, consisting of: (1) a dual-echo three-dimensional (3D)-UTE-Cones sequence (repetition time [TR] = 30 ms; TE = 0.032, 0.2, 0.4, 0.6, 0.8, 2.2, 4.4, 6.6, 8.8, 11, 13 and 15 ms; flip angle [FA] = 10°; rectangular radiofrequency [RF] pulse with a duration of 28 μs) for T_2* measurements (bound and pore water); (2) a variable-TR 3D-UTE-Cones sequence (TE = 0.032 ms; TR = 5.9, 10, 20, 40, 60 and 100 ms; FA = 20°; rectangular RF pulse with a duration of 28 μs) for T_1 measurement; and (3) a 3D-UTE-MT-Cones sequence (MT saturation pulse power = 500°, 750° and 1000°; frequency offset = 2, 5, 10, 20 and 50 kHz; FA = 10°; rectangular RF pulse with a duration of 28 μs) for two-pool MT modelling. Other imaging parameters include a field of view (FOV) = 4 cm, matrix = 192 × 192, slice thickness = 3 mm and receive bandwidth = 62.5 kHz. It should be noted that the nominal TEs are measured from the end of the RF pulse to the start of data sampling. All MRI scans were repeated after the loading experiment. The details of the dual-echo, inversion recovery and variable-TR 3D-UTE-Cones sequences have been discussed in previous studies.[29,30,39,51] The two-pool UTE-MT modeling has been described in detail previously by Ma et al.[33,44] Specifically, the contrast in the two-pool MT model is based on the interactions between macromolecular and water protons.

2.3 | Micro-computed tomography (μCT)

Four fibular samples from the total of 14 were randomly selected and scanned using a Skyscan 1076 (Kontich, Belgium) μCT scanner at an isotropic voxel size of 8.78 μm before and after cyclic loading. This was to examine the μCT capability to detect the microfracture, even though literature has shown that μCT is incapable of detecting microfractures at such a resolution.[18,52] Other scanning parameters were as follows: a 0.05-mm aluminum plus 0.038-mm copper filter, 100 kV, 100 mA, 0.6° rotation step, three frame averaging and 3.5 hours total scan time per sample. Samples were kept humid in a sealed container to avoid dehydration during the μCT scans.

2.4 | Fatigue fracture induction (cyclic loading)

The bone samples were subjected to a cyclic loading session using a four-point bending setup (ASTM D790) to induce a limited fatigue fracture (Figure 2). The jig setup comprised four tungsten pins (3 mm in diameter) held in two aluminum seats. The upper aluminum seat was connected to the actuator and the lower aluminum seat was connected to the load cell. The four-point bending jig was mounted onto a mechanical testing machine (model 8511.20; Instron, Norwood, MA) including a 100-N load cell (Instron 2519–103) with an actuator displacement accuracy of <0.002 mm. The loading was displacement controlled and involved: (1) finding contact; (2) applying approximately −5000 μstrain by manually adjusting the actuator; and (3) applying a sinusoidal displacement to generate −5000 ± 1500 μstrain at 4 Hz. A preconditioning cyclic loading was applied for 1000 cycles before the main loading experiment. The main cyclic loading was stopped by the operator once the monitored bone stiffness (real time measured from strain–stress curves) decreased to below 80% of the initial bone stiffness (elastic modulus). On average, the cyclic loading was stopped after approximately 150 minutes. The schematics of the reduction in measured load as a result of microcracks induced in bone is depicted in Figure 2A.

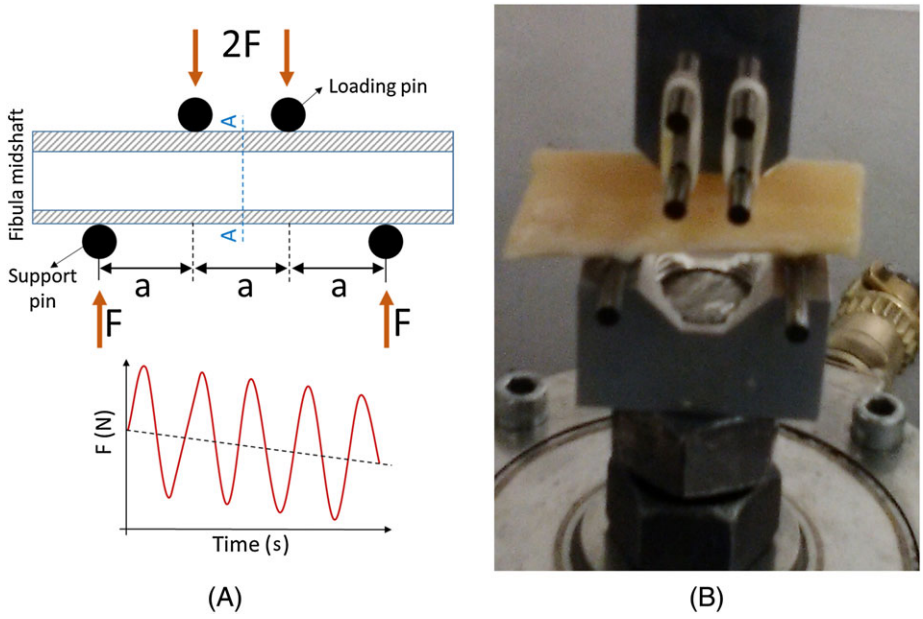

FIGURE 2 Standard four-point bending setup to apply dynamic loads on fibular samples (hollow cylinder) at the midshaft. A, Schematics of the four-point bending jigs at the longitudinal cross-section (a = 8 mm; indenter diameter = 3 mm; fibular diameter = 10 mm approx.). The experiments were displacement controlled (i.e. −5000 ± 1500 μstrain) at 4 Hz and were stopped when 20% reduction in bone stiffness had been achieved (2 hours approx.). A–A is a section between two loading pins, selected for ultrashort echo time-magnetic resonance imaging (UTE-MRI) analyses. B, Prepared fibular midshaft (4 cm approx.) under cyclic mechanical loading using the fabricated four-point bending jigs (aluminum seats and tungsten pins) mounted on an Instron 8511.20 machine

2.5 | Data analysis

MRI data analyses were performed for a selected section (thickness, 3 mm) between the two loading pins (section A–A in Figure 2A) in each of the fibular samples. For each MRI dataset, two regions of interest (ROIs) were selected (Figure 3A) such that A and B covered the compression (upper) and tension (lower) sides of fibular samples in the four-point bending test. Selected ROIs were large enough to avoid being disturbed by pixelwise

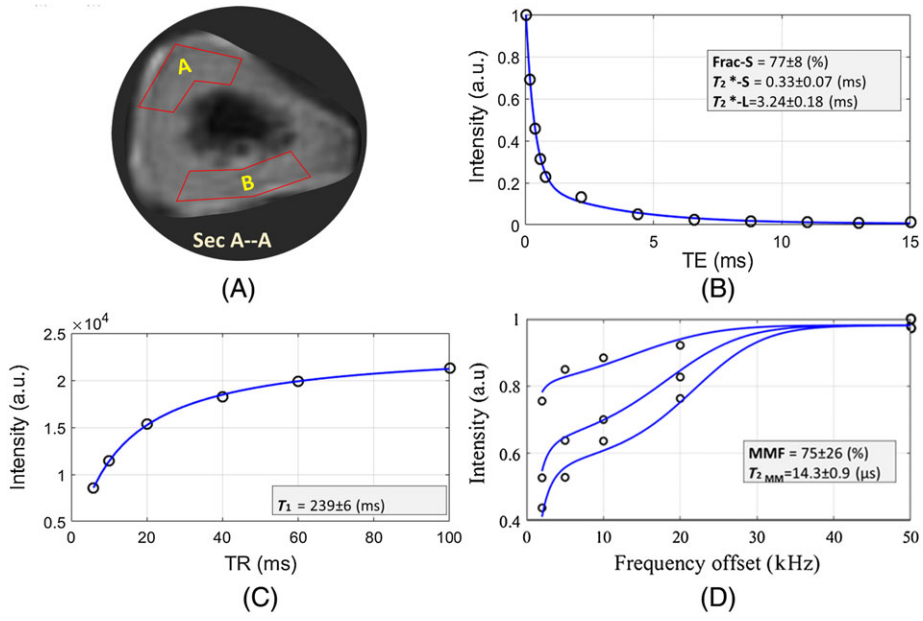

FIGURE 3 The magnetic resonance imaging (MRI)-based analyses for a representative axial section in the middle of sample I (section A–A shown in Figure 2A). The circle points and the solid lines in the subfigures represent the average signal in the region of interest (ROI) and the fitted curves, respectively. A, Two ROIs (A and B) were selected per specimen. ROI A was selected at the compression side in the four-point bending test, whereas ROI B was selected at the tension side. B, Bi-component T_2^* signal decay analyses for differing echo times (TEs) within a representative ROI A (T_2^*-S, T_2^*-L and Frac-S refer to short T_2^*, long T_2^* and fraction of the short T_2^*, respectively). C, T_1 signal recovery analysis for differing repetition times (TR) from 5.7 to 100 ms within the selected ROI. D, The two-pool magnetization transfer (MT) modeling analyses using three pulse saturation powers (500°, 750° and 1000°) and five off-resonance frequencies (2, 5, 10, 20 and 50 kHz). MMF and T_{2MM} refer to the macromolecular fraction and macromolecular T_2, respectively. Excellent fits were obtained for T_1, T_2^* and MT curves for all ROIs

variations in bone specimens (i.e. 120 ± 20 pixels, approximately one-fourth of the total cross-section). Specifically, selected ROIs within post-loading datasets were used to generate ROIs within pre-loading datasets, through an image registration process.

The mean values of single-component T_2^*, bi-component T_2^*, T_1 and MT modelling results within selected ROIs were compared between pre- and post-loading datasets. All data analyses were performed using MATLAB (version 2016, Mathworks, Natick, MA).

2.5.1 | UTE-T_2^* measurements

Single-component $\left(S(\mathrm{TE}) \propto \exp\left(-\mathrm{TE}/T_2^*\right) + \text{constant}\right)$ and bi-component $\left(S(\mathrm{TE}) \propto F_S \times \exp\left(-\mathrm{TE}/T_{2S}^*\right) + F_L \times \exp\left(-\mathrm{TE}/T_{2L}^*\right) + \text{constant}\right)$ fitting models were utilized for T_2^* decay analyses acquired from the dual-echo 3D-UTE-Cones sequence. In contrast with single-component analysis, bi-component analysis of T_2^* provides information on the short T_2^* (bound water) and long T_2^* (pore water) pools, separately.

2.5.2 | UTE-MT measurements

The acquired data with the set of MT saturation pulse powers (500°, 750° and 1000°) and frequency offsets (2, 5, 10, 20 and 50 kHz) were fitted by a modified rectangular pulse (mRP) approximation which has been described previously.[30,53,54] In this model, the loss rate of longitudinal magnetization of the macromolecular pool as a result of RF saturation of the MT pulse is fitted by a Gaussian lineshape function. Consequently, the parameters including MMF and macromolecular T_2 can be estimated as described by Ma et al.[44] As a prerequisite for UTE-MT modeling, T_1 was analyzed from 3D-UTE-Cones images acquired with variable TRs using single-component fitting $\left(S, (\mathrm{TR}) \propto, \left[1 - \exp\left(-\frac{\mathrm{TR}}{T_1}\right)\right], + \text{constant}\right)$. Details of these relaxometry analyses have been provided in previous studies.[29,30,55] The UTE-MT analysis was performed offline on the acquired DICOM images using an in-house code written in MATLAB (version 2016, Mathworks, Natick, MA).

2.5.3 | Bone porosity measurements

The μCT data were processed to calculate the porosity pixel map for an axial 3-mm slice (340 sections, each 8.87 μm thick) of the selected four bone samples. A gray level threshold was used for image segmentation to distinguish between cortical bone and pores. This threshold was selected for each set of data (340 μCT sections) using the peaks of gray level histograms and visual inspection of the raw images. The porosity pixel maps were generated by superimposing all 340 binary images. Affine image registration was used to propagate the ROIs used for MRI analysis to the μCT data.

2.6 | Statistical analysis

All statistical analyses were performed using a statistical programing language (R, version 3.2.5, R Development Core Team, Vienna, Austria). The differences in single-component T_2^*, bi-component T_2^*, T_1 and MT modelling results were compared between pre- and post-loading datasets using a paired Wilcoxon rank-sum test. Shapiro–Wilk test application showed earlier that the data were not normally distributed in this study ($P > 0.05$). The results were specifically compared for average values, compression side and tension side of the fibular samples. P values below 0.05 were considered to be significant.

3 | RESULTS

Figure 3 illustrates the representative MRI-based analyses for a selected axial section (section A–A in Figure 2A) at the middle of sample I. As shown in Figure 3A, the analyses were performed in two ROIs at compression and tension sides (ROI A and ROI B). Figure 3B shows the bi-component T_2^* decay analyses in ROI A. Bi-component analysis provides the T_2^* values and corresponding fractions for bound water and pore water, respectively. Figure 3C illustrates the T_1 recovery using a single-component fitting for variable TRs (5.7–100 ms). MT modeling analysis in ROI A is shown in Figure 3D for three MT saturation pulse powers (500°, 750° and 1000°) and five off-resonance frequencies (2, 5, 10, 20 and 50 kHz).

The summarized results of the single- and bi-component T_2^*, T_1, MT modeling and magnetization transfer ratio (MTR) T_2^* measurements for all fibulae are presented in Table 1 for pre- and post-loading datasets. The average variations of UTE properties by the loading experiments, as well as the corresponding statistical significances (paired Wilcoxon rank-sum test), are presented in Table 2. The variations were calculated for average value per sample, compression side (ROI A) and tension side (ROI B).

For average results, MMF decreased significantly by 12% ± 20% ($P = 0.02$). The MMF reduction was less in compression side ROIs (9% ± 23%, $P = 0.15$) than in tension side ROIs (14% ± 15%, $P = 0.08$). For average results, single-component T_2^* values decreased significantly with the loading experiment, by 12% ± 11% ($P = 0.01$). Single-component T_2^* reduction was higher for compression side ROIs (15% ± 10%, $P = 0.03$) than tension side ROIs (10% ± 11%, $P = 0.28$).

Other UTE-MRI parameters presented noticeable, but not significant, variations, on average, after cyclic loading (Table 2). MTR values reduced, on average, for all selected MT pulse powers and frequency offsets. The MTR variations were higher in tension side ROIs than in compression side ROIs. From bi-component T_2^* analyses, short component T_2^* (T_2^*-S) decreased after loading, on average, whereas its fraction (Frac-S) increased. Long component T_2^* (T_2^*-L) also showed a decrease with loading.

TABLE 1 Average ultrashort echo time-magnetic resonance imaging (UTE-MRI) results (single- and bi-component T_2*, T_1, magnetization transfer [MT] modeling and magnetization transfer ratio [MTR]) for all 14 fibular specimens before and after loading. Compression side refers to the upper side of the fibulae mounted in the four-point bending tests; the tension side refers to the lower side. T_2*-S, T_2*-L and Frac-S refer to short T_2*, long T_2* and fraction of the short T_2*, respectively. MMF is the macromolecular fraction

			Bi-com				MT Model		MTR-500 (%)			MTR-1000 (%)			MTR-1500 (%)		
		T_2* (ms)	Frac-S (%)	T_2*-S (ms)	T_2*-L (ms)	T_1 (ms)	MMF (%)	T_{2MM} (μs)	2 kHz	5 kHz	10 kHz	2 kHz	5 kHz	10 kHz	2 kHz	5 kHz	10 kHz
Average	Pre	0.57 ± 0.23	75 ± 13	0.34 ± 0.04	4.1 ± 1.1	231 ± 35	61 ± 13	15.1 ± 1.3	26 ± 5	14 ± 3	11 ± 2	46 ± 9	32 ± 7	24 ± 5	51 ± 9	39 ± 9	30 ± 7
	Post	0.49 ± 0.16	78 ± 9	0.31 ± 0.05	7.3 ± 13.6	236 ± 34	53 ± 11	14.8 ± 0.9	22 ± 5	12 ± 3	9 ± 3	42 ± 9	30 ± 6	23 ± 5	49 ± 9	37 ± 6	29 ± 5
Compression side	Pre	0.58 ± 0.25	75 ± 13	0.34 ± 0.04	4.2 ± 1.1	245 ± 36	59 ± 15	15.3 ± 1.3	25 ± 6	14 ± 4	10 ± 3	44 ± 10	31 ± 8	24 ± 5	50 ± 11	38 ± 10	29 ± 8
	Post	0.48 ± 0.18	80 ± 10	0.33 ± 0.04	10.9 ± 18.6	244 ± 29	51 ± 9	14.7 ± 0.7	23 ± 6	13 ± 4	10 ± 3	43 ± 10	31 ± 7	23 ± 5	50 ± 9	38 ± 7	29 ± 6
Tension side	Pre	0.57 ± 0.21	75 ± 13	0.33 ± 0.03	4.1 ± 1.1	217 ± 27	64 ± 11	14.8 ± 1.3	27 ± 4	15 ± 2	11 ± 2	47 ± 7	33 ± 5	24 ± 4	53 ± 7	40 ± 7	31 ± 6
	Post	0.50 ± 0.14	77 ± 8	0.29 ± 0.06	3.7 ± 1.0	228 ± 36	55 ± 12	14.9 ± 1.1	22 ± 5	12 ± 3	9 ± 2	42 ± 8	30 ± 5	23 ± 4	48 ± 8	37 ± 6	29 ± 5

TABLE 2 Summarized variations (mean ± standard deviation) in analyzed ultrashort echo time-magnetic resonance imaging (UTE-MRI)-based biomarkers (single-component T_2*, bi-component T_2*, T_1, magnetization transfer [MT] modeling and magnetization transfer ratio [MTR]) by cyclic loading experiment. Compression side refers to the upper side of the fibulae mounted in the four-point bending tests; the tension side refers to the lower side. The positive and negative signs indicate the increases and decreases, respectively. T_2*-S, T_2*-L and Frac-S refer to short T_2*, long T_2* and fraction of the short T_2*, respectively. MMF is the macromolecular fraction. All changes are percentages

		Bi-com				MT Model		MTR-500			MTR-1000			MTR-1500		
	T_2*	Frac-S	T_2*-S	T_2*-L	T_1	MMF	T_{2MM}	2 kHz	5 kHz	10 kHz	2 kHz	5 kHz	10 kHz	2 kHz	5 kHz	10 kHz
Average	−12 ± 11 P = 0.01	+7 ± 15 P = 0.38	−7 ± 16 P = *0.70*	+68 ± 269 P = 0.20	+3 ± 13 P = 0.66	−12 ± 20 P = 0.02	−2 ± 5 P = 0.24	−12 ± 20 P = *0.05*	−13 ± 20 P = 0.11	−10 ± 22 P = 0.22	−6 ± 16 P = 0.29	−3 ± 17 P = 0.31	−2 ± 16 P = 0.84	−3 ± 15 P = 0.55	−3 ± 16 P = 0.41	0 ± 19 P = 0.51
Compression side	−15 ± 10 P = 0.03	+7 ± 11 P = 0.40	−3 ± 14 P = *0.71*	+141 ± 365 P = 0.12	0 ± 13 P = 0.70	−9 ± 23 P = 0.15	−4 ± 5 P = 0.19	−9 ± 18 P = *0.19*	−8 ± 20 P = 0.37	−5 ± 22 P = 0.48	−2 ± 13 P = 0.77	1 ± 16 P = 0.84	−1 ± 16 P = 0.91	2 ± 13 P = 0.87	+1 ± 14 P = 0.98	+5 ± 17 P = 0.95
Tension side	−10 ± 11 P = 0.28	+6 ± 19 P = 1.00	−11 ± 17 P = *0.36*	−5 ± 33 P = 0.57	+5 ± 13 P = 0.30	−14 ± 15 P = 0.08	1 ± 5 P = 0.76	−15 ± 21 P = *0.01*	−18 ± 18 P = 0.02	−14 ± 21 P = 0.05	−10 ± 17 P = 0.07	−7 ± 17 P = 0.28	−4 ± 17 P = 0.68	−8 ± 16 P = 0.12	−7 ± 17 P = 0.22	−4 ± 19 P = 0.40

Figure 4 shows MMF and single-component T_2^* pixel maps of a representative sample (i.e. sample I) for pre- and post-loading datasets. The anticipated reductions in MMF and T_2^* values from Tables 1 and 2 are obvious in the depicted maps.

Table 3 presents the μCT-based porosities of the four selected fibular samples for pre- and post-loading datasets. The average porosity varied from 1.8% ± 0.6% to 1.6% ± 0.7% (P = 0.89). The porosity varied from 1.2% ± 0.6% to 1.6% ± 0.9% (P = 0.49) and from 2.4% ± 1.1% to 1.6% ± 1.2% (P = 0.17) for compression and tension side ROIs, respectively. All μCT-based porosity variations were found to be nonsignificant.

4 | DISCUSSION

UTE-MRI-based biomarkers were studied, for the first time, to detect partial fatigue fractures in cortical bone, as an early stage of BSI. UTE-MRI has been used by different research groups to assess cortical bone microstructural and mechanical properties.[29,30,34,41,42,45,47-50] However, UTE-MRI has not been used for bone fatigue fracture detection.

Conventional radiography, CT, musculoskeletal ultrasonography, scintigraphy and MRI are clinical techniques that have been used to detect BSI. Conventional radiographs, as the first routine imaging modality, may detect BSI at 2–12 weeks after onset. The first radiographic sign is a low-density area in cortical bone. The sensitivity of radiography is 15%–35% in the early stages of BSI.[1,6,13,16,22-24] CT may be less sensitive than conventional radiography for the diagnosis of BSI. However, certain fracture lines can be seen more clearly with CT.[13,16,22-24] Scintigraphy (radionuclide bone scan) has been considered to be the best diagnostic method for BSI, with a reported sensitivity close to 100%, but with high false

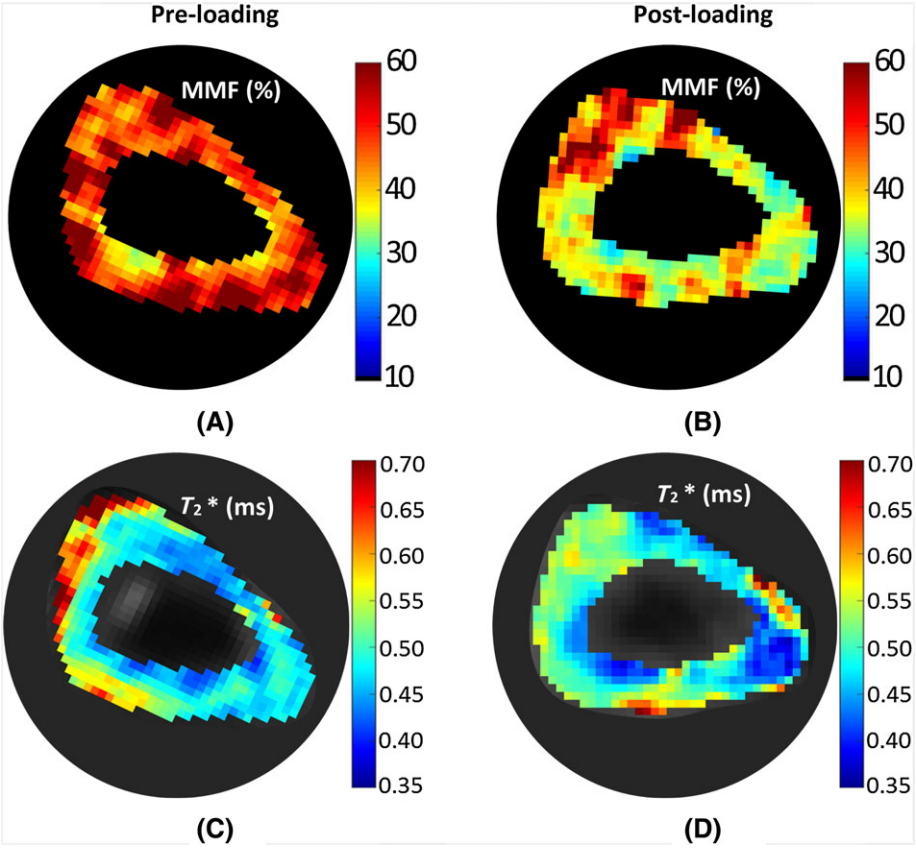

FIGURE 4 Pixel maps of macromolecular fraction (MMF) (A,B) and single-component T_2^* (C,D) for a representative sample (sample I) at pre- and post-loading stages. These two parameters present significant variation, on average, with ex vivo bone stress injury (BSI) (Table 2). MMF and T_2^* decreases are obvious in the whole section of sample I

TABLE 3 Average micro-computed tomography (μCT)-based porosities for four representative fibular specimens in different regions of interest (ROIs) at compression and tension sides in the four-point bending test. All values are percentages

	Pre-loading				Post-loading			
Sample	I	II	III	IV	I	II	III	IV
Average	1.9	2.5	1.7	1.0	2.1	2.3	0.7	1.2
Compression side	2.2	0.9	1.1	0.7	3.0	1.13	0.9	1.3
Tension side	1.6	4.0	2.9	1.3	1.2	3.5	0.3	1.2

positive diagnosis.[1,6,13,16,23,24,56] Scintigraphy can show an increase in bone uptake as early as 6 − 72 hours after the onset of pain.[1,6,13,16,23,24] The high radiation dose in scintigraphy is another important concern in addition to the high false diagnosis rate.[24] Musculoskeletal ultrasonography for BSI diagnosis remains in an early investigation stage.[13,24]

Clinical MRI (e.g. T_1-weighted and fluid-sensitive images) has been recommended for the detection of early-stage BSI, through observations of edema in and around the periosteum and bone marrow.[1,13] Fredericson et al.[57] developed a grading approach for BSI (four grades) based on the edema observations in MRI. Later, Kijowski et al.[27] improved and simplified the Fredericson grades based on the return to play time. They suggested combining three of the grades that have similar degrees of periosteum and bone marrow edema and similar time to return (two instead of four grades). Semi-quantitative approaches (grading) have been the most systematic methods in the MRI-based diagnosis of BSI[1,10,13,27,28]; however, these grades fail to quantify the extent of injury to the bone.

All hypothesized mechanisms for BSI may end in collagenous matrix rupture and bone microcracks at the early stages. Such microcracks may occur at different scales: microstructural and ultrastructural.[17,18] At the microstructural level, cracks can be 20–100 μm in length in the transverse plane of cortical bone, and reach 500–1000 μm in the longitudinal plane (88 ± 21 and 488 ± 151 μm width and length, respectively[17]). However, the thickness of microcracks may only be a few micrometers. At the ultrastructural level, numerous nanocracks may be grouped and result in short arrays (<10 μm in length) visible on histology images.[18] Fatigue fractures accompany the reduction in bone stiffness and initiate with cracks at the ultrastructural level, which later evolve into cracks at the microstructural level.[18,52]

Our cyclic loading experiment led to partial fatigue fracture in cortical bone that resembled the early stages of BSI. The fatigue fracture was implied by the 20% reduction in monitored bone stiffness. As reported in the literature, the bone stiffness reduction via cyclic loading is always accompanied by the presence of microcracks.[52,58-61] A few UTE-MRI quantitative properties of post-loading bone samples demonstrated significant changes compared with pre-loading samples.

MMF, from two-pool MT modelling, presented a significant reduction, on average, in bone specimens after loading (12% ± 20%, P = 0.02, Table 2). The MMF reduction was higher for tension side ROIs than compression side ROIs (14% ± 15% versus 9% ± 23%, Table 2). Significant MMF reduction probably indicates collagenous matrix rupture or collagen softening. Probable higher water loss in compression side ROIs is expected to downgrade the MMF variations. MTR reductions by the induced fatigue fracture also imply collagenous matrix rupture, although the variations were not significant (Table 2). More sophisticated analyses of the MT signal, such as the presented UTE-MT modeling, demonstrated a stronger potential to sense the complex nature of BSI, which is not limited to water redistribution or collagenous matrix rupture.

Single-component T_2^* decreased significantly in the bone samples (12% ± 11%, P = 0.01, Table 2). T_2^*-S from bi-component analyses decreased after loading, on average, but its fraction (Frac-S) increased. Long component T_2^* (T_2^*-L) also showed a decrease with loading. Such T_2^* reductions most likely demonstrate water shifts towards the generated micro- and nanocracks with higher susceptibility, which, in turn, result in faster T_2^* decay.

The μCT-based porosity variation in four selected specimens was not statistically significant or consistent (Table 3). Indeed, μCT at a voxel size of 8.78 μm was limited to detect not only the micro- and nanocracks, but also many of the original pores in cortical bone. Specifically, the cracks induced by cyclic loading, resulting in a 20% reduction in bone stiffness, were expected to be at the ultrastructural level, which may not be detectable by μCT. In the same way, Burr et al.[52] did not observe significant microdamage at the light microscopy level (submicrometer pixel size) until there was a 15% decrease in canine bone stiffness.[18,52] However, Landrigan et al.[60] and Turnbull et al.[61] were able to detect microcracks induced by 5%–10% reduction in bone stiffness using a μCT dataset at a voxel size of 10 μm, but only when barium sulfate (BaSO4) contrast agent was administered.

Our results indicate that quantitative UTE-MT-MRI has great potential to serve as a new diagnostic technique for BSI at an early stage (i.e. fatigue fracture). The quantitative UTE-MT-MRI technique, complemented with clinical MRI (to detect edema in surrounding soft tissue), could be an accurate and comprehensive diagnostic method, and deserves further study. UTE-MT modeling results, particularly MMF, were found to vary significantly in damaged locations of cortical bone.

In vivo BSI is expected to be slightly different from the ex vivo BSI presented in this study. The response from the peripheral soft tissue environment, as well as the biological and immune system, would be to enhance cellular activities, uptake and intraosseous hydrostatic pressures.[1] Such enhancements can explain the development of edema around injured bone in patients.[1,13] Moreover, the cellular resorption process, triggered by the excessive loading in bone, is expected to initiate BSI.[1,4,56] All the aforementioned phenomena are expected to result in higher water concentration around injured in vivo bone. Thus, a larger MMF reduction is anticipated for in vivo BSI compared with the observed reductions in this study for ex vivo BSI.

A constant offset was introduced into the fitting models which may lead to an overestimation of the relaxation times because of the Rician-distributed noise contribution. However, the noise distribution in 3D-UTE images is more complicated than in conventional Cartesian images. Streak artifacts associated with spiral sampling may affect the noise distribution. The introduction of a constant term seems to be helpful to account for the contribution from artifacts associated with spiral sampling and imperfect regridding reconstruction. The consideration of a constant contribution of noise to the MRI signal might lead to a slight overestimation of the relaxation times in this study. Nonetheless, the overestimations are consistent and can be neglected when the variation of the relaxation times is the focus of the study.

This study has several limitations as follows. First, the fibular samples possessed a variety of shapes that may not be perfectly mounted on the four-point bending jigs. Therefore, the load might not be distributed evenly between pins (Figure 2A) for all samples, which may challenge the accurate localization of anticipated fractures. The preparation of rectangular slabs of cortical bone from tibia for future studies is recommended.

Second, the level of the induced microdamage in bone was not sufficient to be detected in μCT at a voxel size of 9 μm. Further studies should investigate higher levels of bone stiffness reduction with higher μCT resolution, probably with contrast agents, in addition to histological studies. Three-dimensional histomorphometric measures of microcracks (number and volume) should be correlated with the UTE-MRI biomarkers, as well as the induced BSI severity level, to determine which combination of parameters can provide the highest sensitivity and specificity for BSI diagnosis. Indeed, the MRI properties are not independent from each other, and an optimum combination might be practical to assess BSI. Third, this study was performed on ex vivo cortical bone and lacked the peripheral soft tissue environment, as well as biological and immune system reactions, after fatigue fracture incidence. Thus, the presented results and hypotheses need to be validated in a well-designed in vivo animal model or human study.

5 | CONCLUSIONS

UTE-MRI was used, for the first time, to detect fatigue fracture in cortical bone in an ex vivo study. UTE-MRI-based biomarkers in fibular samples changed significantly after cyclic loading, which induced fatigue fracture in bone samples. MMF, from MT modeling outputs, significantly decreased with ex vivo BSI. MMF reduction most probably resulted from collagenous matrix rupture. Single-component T_2^* values of bone samples demonstrated a significant decrease, which probably implies water shifts towards the generated micro- and nanocracks with higher susceptibility, which, in turn, results in faster T_2^* decay. As expected, μCT performed on the representative specimens was not sensitive to the fatigue fracture at the examined resolution. UTE-MT modeling was found to be capable of detecting fatigue fracture in cortical bone. UTE-MT may be recommended as a complementary technique to improve the accuracy and precision of BSI diagnosis at an early stage.

ACKNOWLEDGEMENTS

The authors thank Niloofar Shojaeiadib for performing the statistical analyses. The authors acknowledge grant support from the National Institutes of Health (NIH) (5 P01 AG007996, 1 R01 AR062581-01A1 and 1 R01 AR068987-01) and VA (I01CX001388).

CONFLICTS OF INTEREST

The authors have no conflicts of interest to declare.

ORCID

Saeed Jerban http://orcid.org/0000-0001-6450-2892
Jiang Du http://orcid.org/0000-0002-9203-2450

REFERENCES

1. Lassus J, Tulikoura I, Konttinen YT, Salo J, Santavirta S. Bone stress injuries of the lower extremity: a review. *Acta Orthop Scand*. 2002;73(3):359-368.
2. Welck MJ, Hayes T, Pastides P, Khan W, Rudge B. Stress fractures of the foot and ankle. *Injury*. 2015;48(8):1722-1726.
3. Magnotti T. How serious are stress fractures for NBA players? http://hoopshabit.com/2014/06/23/serious-stress-fractures-nba-players/. 2014. Accessed June 2017.
4. Romani WA, Gieck JH, Perrin DH, Saliba EN, Kahler DM, Anonymous. Mechanisms and management of stress fractures in physically active persons. *J Athl Train*. 2002;37(3):306-314.
5. Behrens SB, Deren ME, Matson A, Fadale PD, Fadale KO. Stress fractures of the pelvis and legs in athletes: a review. *Sports Health*. 2013;5(2):165-174.
6. Mayer SW, Joyner PW, Almekinders LC, Parekh SG. Stress fractures of the foot and ankle in athletes. *Sports Health*. 2013;6(6):481-491.
7. Kiuru MJ, Pihlajamäki HK, Ahovuo JA. Bone stress injuries. *Acta Radiol*. 2004;45(3):317-326.
8. Reinking MF, Austin TM, Bennett J, Hayes AM, Mitchell WA. Lower extremity overuse bone injury risk factors in collegiate athletes: a pilot study. *Int J Sports Phys Ther*. 2015;10(2):155-167. http://www.pubmedcentral.nih.gov/articlerender.fcgi?artid=4387723&tool=pmcentrez&rendertype=abstract. Accessed June 2017.
9. Barrack MT, Gibbs JC, De Souza MJ, et al. Higher incidence of bone stress injuries with increasing female athlete triad – related risk factors. *Am J Sports Med*. 2014;42(4):949-958.
10. Nattiv A, Kennedy G, Barrack MT, et al. Correlation of MRI grading of bone stress injuries with clinical risk factors and return to play: a 5-year prospective study in collegiate track and field athletes. *Am J Sports Med*. 2013;41(8):1930-1941.
11. Lee K, Park Y, Jegal H, Kim K, Young K, Kim J. Factors associated with recurrent fifth metatarsal stress fracture. *Foot Ankle Int*. 2013;34(12):1645-1653.
12. Bui-Mansfield LT, Thomas WR. Magnetic resonance imaging of stress injury of the cuneiform bones in patients with plantar fasciitis. *J Comput Assist Tomogr*. 2009;33(4):593-596.
13. McInnis KC, Ramey LN. High-risk stress fractures: diagnosis and management. *Phys Med Rehabil*. 2016;8(3,suppl):S113-S124.
14. Armstrong DW, Rue JPH, Wilckens JH, Frassica FJ. Stress fracture injury in young military men and women. *Bone*. 2004;35(3):806-816.
15. Anderson MW, Greenspan A. Stress fractures. *Radiol Clin North Am*. 1996;1999:1-12.
16. Asano L, Duarte J, Silva APS. Stress fractures in the foot and ankle of athletes. *Rev Assoc Med Bras*. 2014;60(6):512-517.
17. Mohsin S, O'Brien FJ, Lee TC. Microcracks in compact bone: a three-dimensional view. *J Anat*. 2006;209(1):119-124.

18. Donahue SW, Galley SA. Microdamage in bone: implications for fracture, repair, remodeling, and adaptation. *Crit Rev Biomed Eng*. 2006;34(3):215-271.
19. Niva MH, Sormaala MJ, Kiuru MJ. Bone stress injuries of the ankle and foot an 86-month magnetic resonance imaging-based study of physically active young adults. *Am J Sports Med*. 2007;35(4):643-649.
20. Hong SH, Chu IT. Stress fracture of the proximal fibula in military recruits. *Clin Orthop Surg*. 2009;1(3):161-164.
21. Wilson ES, Katz FN. Stress fractures. *Radiology*. 1969;92(March):481-486.
22. Astur DC, Zanatta F, Arliani GG, Moraes ER, de Pochini AC, Ejnisman B. Stress fractures: definition, diagnosis and treatment. *Rev Bras Ortop (English Ed)*. 2016;51(1):3-10.
23. Patel DS, Roth M, Kapil N. Stress fractures: diagnosis, treatment, and prevention. *Am Fam Physician*. 2011;83(1):39-46.
24. Pegrum J, Crisp T, Padhiar N. Diagnosis and management of bone stress injuries of the lower limb in athletes. *BMJ*. 2012;344(apr24 3):e2511-e2511.
25. Gmachowska A, Zabicka M, Pacho R. MRI findings of tibial stress injuries. *Eur Soc Radiol*. 2014;C-1507:1-26.
26. Gaeta M, Minutoli F, Scribano E, et al. CT and MR imaging findings in athletes with early tibial stress injuries: comparison with bone scintigraphy findings and emphasis on cortical abnormalities. *Radiology*. 2005;235(2):553-561.
27. Kijowski R, Choi J, Shinki K, Del Rio AM, De Smet A. Validation of MRI classification system for tibial stress injuries. *Am J Roentgenol*. 2012;198(4):878-884.
28. Ruohola J-PS, Kiuru MJ, Pihlajamäki HK. Fatigue bone injuries causing anterior lower leg pain. *Clin Orthop Relat Res*. 2006;444(444):216-223.
29. Chang EY, Du J, Chung CB. UTE imaging in the musculoskeletal system. *J Magn Reson Imaging*. 2015;41(4):870-883.
30. Du J, Bydder GM. Qualitative and quantitative ultrashort-TE MRI of cortical bone. *NMR Biomed*. 2013;26(5):489-506.
31. Diaz E, Chung CB, Bae WC, et al. Ultrashort echo time spectroscopic imaging (UTESI): an efficient method for quantifying bound and free water. *NMR Biomed*. 2012;25(1):161-168.
32. Du J, Carl M, Bydder M, Takahashi A, Chung CB, Bydder GM. Qualitative and quantitative ultrashort echo time (UTE) imaging of cortical bone. *J Magn Reson*. 2010;207(2):304-311.
33. Ma Y-J, Shao H, Du J, Chang EY. Ultrashort echo time magnetization transfer (UTE-MT) imaging and modeling: magic angle independent biomarkers of tissue properties. *NMR Biomed*. 2016;29(11):1546-1552.
34. Rajapakse CS, Bashoor-Zadeh M, Li C, Sun W, Wright AC, Wehrli FW. Volumetric cortical bone porosity assessment with MR imaging: validation and clinical feasibility. *Radiology*. 2015;276(2):526-535.
35. Seifert AC, Wehrli FW. Solid-state quantitative ^{1}H and ^{31}P MRI of cortical bone in humans. *Curr Osteoporos Rep*. 2016;14(3):77-86.
36. Granke M, Does MD, Nyman JS. The role of water compartments in the material properties of cortical bone. *Calcif Tissue Int*. 2015;97(3):292-307.
37. Manhard MK, Horch RA, Harkins KD, Gochberg DF, Nyman JS, Does MD. Validation of quantitative bound- and pore-water imaging in cortical bone. *Magn Reson Med*. 2014;71(6):2166-2171.
38. Nyman JS, Ni Q, Nicolella DP, Wang X. Measurements of mobile and bound water by nuclear magnetic resonance correlate with mechanical properties of bone. *Bone*. 2008;42(1):193-199.
39. Du J, Hermida JC, Diaz E, et al. Assessment of cortical bone with clinical and ultrashort echo time sequences. *Magn Reson Med*. 2013;70(3):697-704.
40. Jerban S, Nazaran A, Cheng X, et al. Ultrashort echo time T2* values decrease in tendons with application of static tensile loads. *J Biomech*. 2017;61:160-167.
41. Li C, Seifert AC, Rad HS, et al. Cortical bone water concentration: dependence of MR imaging measures on age and pore volume fraction. *Radiology*. 2014;272(3):796-806.
42. Horch RA, Gochberg DF, Nyman JS, Does MD. Clinically compatible MRI strategies for discriminating bound and pore water in cortical bone. *Magn Reson Med*. 2012;68(6):1774-1784.
43. Larson PEZ, Conolly SM, Pauly JM, Nishimura DG. Using adiabatic inversion pulses for long-T2 suppression in ultrashort echo time (UTE) imaging. *Magn Reson Med*. 2007;58(5):952-961.
44. Ma Y-J, Chang EY, Carl M, Du J. Quantitative magnetization transfer ultrashort echo time imaging using a time-efficient 3D multispoke Cones sequence. *Magn Reson Med*. 2018;79(2):692-700.
45. Chang EY, Bae WC, Shao H, et al. Ultrashort echo time magnetization transfer (UTE-MT) imaging of cortical bone. *NMR Biomed*. 2015;28(April):873-880.
46. Li S, Chang EY, Bae WC, et al. Ultrashort echo time bi-component analysis of cortical bone - a field dependence study. *Magn Reson Med*. 2014;71(3):1075-1081.
47. Bae WC, Chen PC, Chung CB, Masuda K, D'Lima D, Du J. Quantitative ultrashort echo time (UTE) MRI of human cortical bone: correlation with porosity and biomechanical properties. *J Bone Miner Res*. 2012;27(4):848-857.
48. Rad HS, Lam SCB, Magland JF, et al. Quantifying cortical bone water in vivo by three-dimensional ultra-short echo-time MRI. *NMR Biomed*. 2011;24(7):855-864.
49. Horch RA, Gochberg DF, Nyman JS. Does MD. Non-invasive predictors of human cortical bone mechanical properties: T2-discriminated ^{1}H NMR compared with high resolution X-ray. *PLoS One*. 2011;6(1):1-5.
50. Chen J, Grogan SP, Shao H, et al. Evaluation of bound and pore water in cortical bone using ultrashort-TE MRI. *NMR Biomed*. 2015;28(12):1754-1762.
51. Nazaran A, Carl M, Ma Y-J, et al. Three-dimensional adiabatic inversion recovery prepared ultrashort echo time cones (3D IR-UTE-Cones) imaging of cortical bone in the hip. *Magn Reson Imaging*. 2017;44:60-64.
52. Burr DB, Turner CH, Naick P, et al. Does microdamage accumulation affect the mechanical properties of bone? *J Biomech*. 1998;31(4):337-345.
53. Ma Y-J, Tadros A, Du J, Chang EY. Quantitative two-dimensional ultrashort echo time magnetization transfer (2D UTE-MT) imaging of cortical bone. *Magn Reson Med*.
54. Ramani A, Dalton C, Miller DH, Tofts PS, Barker GJ. Precise estimate of fundamental in vivo MT parameters in human brain in clinically feasible times. *Magn Reson Imaging*. 2002;20(10):721-731.

55. Biswas R, Bae WC, Diaz E, et al. Ultrashort echo time (UTE) imaging with bi-component analysis: bound and free water evaluation of bovine cortical bone subject to sequential drying. *Bone*. 2012;50(3):749-755.

56. Peris P. Stress fractures. *Best Pract Res Clin Rheumatol*. 2003;17(6):1043-1061.

57. Fredericson M, Bergman AG, Hoffman KL, Dillingham MS. Tibial stress reaction in runners: correlation of clinical symptoms and scintigraphy with a new magnetic resonance imaging grading system. *Am J Sports Med*. 1995;23(4):472-481.

58. Pattin CA, Caler WE, Carter DR. Cyclic mechanical property degradation during fatigue loading of cortical bone. *J Biomech*. 1996;29(1):69-79.

59. Diab T, Vashishth D. Effects of damage morphology on cortical bone fragility. *Bone*. 2005;37(1):96-102.

60. Landrigan MD, Li J, Turnbull TL, Burr DB, Niebur GL, Roeder RK. Contrast-enhanced micro-computed tomography of fatigue microdamage accumulation in human cortical bone. *Bone*. 2011;48(3):443-450.

61. Turnbull TL, Gargac JA, Niebur GL, Roeder RK. Detection of fatigue microdamage in whole rat femora using contrast-enhanced micro-computed tomography. *J Biomech*. 2011;44(13):2395-2400.

How to cite this article: Jerban S, Ma Y, Nazaran A, et al. Detecting stress injury (fatigue fracture) in fibular cortical bone using quantitative ultrashort echo time-magnetization transfer (UTE-MT): An ex vivo study. *NMR in Biomedicine*. 2018;31:e3994. https://doi.org/10.1002/nbm.3994